Title

Phospholipid methylation regulates muscle metabolic rate through Ca2+ transport efficiency

Journal

Nature Metabolism, 1(9)

ISSN

2522-5812

Authors

Verkerke, Anthony RP
Ferrara, Patrick J
Lin, Chien-Te
et al.

Publication Date

2019-09-01

DOI

10.1038/s42255-019-0111-2

Peer reviewed

HHS Public Access

Author manuscript

Nat Metab. Author manuscript; available in PMC 2020 May 13.

Published in final edited form as:

Nat Metab. 2019 September ; 1(9): 876–885. doi:10.1038/s42255-019-0111-2.

Phospholipid methylation regulates muscle metabolic rate through Ca^{2+} transport efficiency

Anthony R.P. Verkerke[1,2], **Patrick J. Ferrara**[1,2], **Chien-Te Lin**[3], **Jordan M. Johnson**[1,2], **Terence E. Ryan**[4], **J. Alan Maschek**[5], **Hiroaki Eshima**[1], **Christopher W. Paran**[3], **Brenton T. Laing**[3], **Piyarat Siripoksup**[1,6], **Trevor S. Tippetts**[1,2], **Edward J. Wentzler**[3], **Hu Huang**[3], **Espen. E. Spangenburg**[3], **Jeffrey J. Brault**[3], **Claudio J. Villanueva**[1,7], **Scott A. Summers**[1,2,9], **William L. Holland**[1,2,9], **James E. Cox**[1,5,7], **Dennis E. Vance**[8], **P. Darrell Neufer**[3], **Katsuhiko Funai**[1,2,3,6,9,*]

[1]Diabetes & Metabolism Research Center, University of Utah, Salt Lake City, Utah, USA

[2]Department of Nutrition & Integrative Physiology, University of Utah, Salt Lake City, Utah, USA

[3]East Carolina Diabetes and Obesity Institute, East Carolina University, Greenville, North Carolina, USA

[4]Department of Applied Physiology and Kinesiology, University of Florida, Gainesville, Florida, USA

[5]Metabolomics Core Research Facility, University of Utah, Salt Lake City, Utah, USA

[6]Department of Physical Therapy & Athletic Training, University of Utah, Salt Lake City, Utah, USA

[7]Department of Biochemistry, University of Utah, Salt Lake City, Utah, USA

[8]Department of Biochemistry, University of Alberta, Edmonton, Alberta, Canada

[9]Molecular Medicine Program, University of Utah, Salt Lake City, Utah, USA

Abstract

The biophysical environment of membrane phospholipids affects structure, function, and stability of membrane-bound proteins.[1,2] Obesity can disrupt membrane lipids, and in particular, alter the activity of sarco/endoplasmic reticulum (ER/SR) Ca^{2+}-ATPase (SERCA) to affect cellular

*Corresponding Author: Katsuhiko Funai, Ph.D., Diabetes & Metabolism Research Center, 15 N 2030 E, Salt Lake City, UT 84112, Phone: (801) 585-1781, Fax: (801) 585-0701, kfunai@utah.edu.

Author Contributions

A.R.P.V. and K.F. designed the study and wrote the manuscript. A.R.P.V. performed all metabolic phenotyping and biochemical assays. A.R.P.V., P.J.F., and E.E.S. performed muscle oxygen consumption assays. C.L., J.M.J., T.E.R., and P.D.N. performed mitochondrial phenotyping. H.E. and P.S. assisted in muscle histology and functional measurements. C.J.V. assisted in experiments with adipose tissues. T.S.T., S.A.S., and W.L.H. assisted in AAV experiments. J.A.M. and J.E.C. performed mass spectrometry analyses. A.R.P.V. and J.J.B performed ultra-performance liquid chromatography. B.T.L and H.H. performed analyses on hypothalamus. A.R.P.V., C.W.P., E.J.W., D.E.V., and K.F. designed and generated the mouse models. T.E.R., H.H., E.E.S., J.J.B., S.A.S., W.L.H., J.E.C., D.E.V., and P.D.N. edited the manuscript.

Competing Interests

The authors declare no competing financial interests.

metabolism.[3–5] Recent evidence suggests that transport efficiency (Ca^{2+} uptake / ATP hydrolysis) of skeletal muscle SERCA can be uncoupled to increase energy expenditure and protect mice from diet-induced obesity.[6,7] In isolated SR vesicles, membrane phospholipid composition is known to modulate SERCA efficiency.[8–11] Here we show that skeletal muscle SR phospholipids can be altered to decrease SERCA efficiency and increase whole-body metabolic rate. The absence of skeletal muscle phosphatidylethanolamine (PE) methyltransferase (PEMT) promotes an increase in skeletal muscle and whole-body metabolic rate to protect mice from diet-induced obesity. The elevation in metabolic rate is caused by a decrease in SERCA Ca^{2+}-transport efficiency, whereas mitochondrial uncoupling is unaffected. Our findings support the hypothesis that skeletal muscle energy efficiency can be reduced to promote protection from obesity.

Genome-wide association data has identified PEMT polymorphism to be associated with obesity,[12] and whole-body deletion of PEMT (PEMTKO) protects mice from high-fat diet (HFD)-induced weight gain.[13] PEMTKO mice exhibit increased whole-body energy expenditure with no known mechanism.[14] Raised at thermoneutrality (29°C) or room temperature, HFD-fed wild-type (WT) and PEMTKO mice were systematically evaluated. Consistent with previous reports, PEMTKO mice were protected from diet-induced weight gain (Fig. 1a, Supplementary Fig. 1a–e) without a decrease in food consumption (Fig. 1b), representing metabolic inefficiency (Supplementary Fig. 1f). Indirect calorimetry showed that PEMTKO mice demonstrated increased whole-body VO_2 (Fig. 1c, Supplementary Fig. 1g&h) in the absence of increased spontaneous activity (Fig. 1d). Increased metabolic rate was not explained by differences in abundance of hypothalamic POMC or AgRP/NPY-expressing neurons (Fig. 1e, Supplementary Fig. 1i&j), or increases in thyroid hormones (Fig. 1f), ruling out these systemic mechanisms. A previous study showed no increase in UCP1 protein in brown adipose tissue,[15] and we could not detect any UCP1 proteins in subcutaneous or visceral white adipose tissues (Fig. 1g&h), nor could we detect thermogenic reprograming in subcutaneous or visceral white adipose tissues (Supplementary Fig. 1k&l). Skeletal muscle is a major contributing tissue to total energy expenditure.[12] Muscles from PEMTKO mice show a modest change in mitochondrial morphology without an increase in oxidative capacity.[14] To evaluate the basal metabolic rate of skeletal muscle, we measured oxygen consumption of isolated extensor digitorum longus (EDL) muscles suspended *ex vivo* (mVO_2).[16] Strikingly, resting mVO_2 was ~40% greater in PEMTKO mice compared to WT mice (Fig. 1i&j). To rule out a possibility that the differences in mVO_2 came from differences in O_2 transport gradient in the muscle, we measured O_2 consumption in cultured intact muscle fibers from flexor digitorum brevis (FDB) muscle using a Seahorse platform. Basal O_2 consumption rate in muscle fibers from PEMTKO mice was also ~40% greater compared to WT mice (Fig. 1k&l). Assessment of high-energy phosphates suggested that muscles deficient in PEMT may be in a state of accelerated ATP supply (Supplementary Fig. 1m&n). As muscle accounts for 20–30% of resting whole-body energy expenditure, it can be deduced that 8–12% out of the ~15% increase in whole-body energy expenditure (Fig. 1c) is accounted for by an increase in basal mVO_2. The remaining difference is also likely largely accounted for by muscle energy expenditure when mice are active, making it somewhat unlikely that other tissues substantially contribute to greater whole-body metabolic rate in PEMTKO mice.

What is the molecular mechanism by which absence of PEMT increases skeletal muscle energy expenditure? Skeletal muscle mitochondria can be proton-uncoupled to be energetically inefficient which can protect mice from diet-induced obesity.[17,18] Oligomycin-treated oxygen consumption rates (proton leak-dependent respiration) were not different between WT and PEMTKO fibers (Fig. 2a), but we performed high-resolution respirometry and fluorometry experiments to more carefully phenotype mitochondria. Nevertheless, respiratory efficiency of mitochondria (ATP produced / O_2 reduced, or P/O ratio; Fig. 2b, Supplementary Fig. 2a–c), proton leak measured at multiple membrane potentials (Fig. 2c), or electron leak estimated with superoxide production (Fig. 2d, Supplementary Fig. 2d) were not different between WT and PEMTKO mice. There was a modest increase in glutathione buffering capacity (Supplementary Fig. 2e–g) in muscles from PEMTKO mice, suggesting that these mitochondria may be more adept to oxidative challenge. Consistent with previous reports,[14] we did not observe any differences in skeletal muscle respiratory capacity (Supplementary Fig. 2h&i) or mitochondrial content (Supplementary Fig. 2j&k). It is important to note that cellular work (ΔG_{ATP}), not capacity, drives the metabolic rate. Thus, it is unsurprising that the increase in endogenous activity of mitochondrial oxidative phosphorylation occurs independent of an increase in oxidative capacity. Together, these data suggest that alteration in skeletal muscle mitochondrial efficiency or capacity does not explain the increased metabolic rate in PEMT-deficient muscles.

The lack of robust phenotype in skeletal muscle mitochondria is not surprising given that PEMT is located in ER,[19] and PEMT deletion does not affect skeletal muscle mitochondrial membrane phospholipid composition.[14] Instead, absence of PEMT affected phospholipid composition of muscle SR (Fig. 2e&f, Supplementary Fig. 2l&m) and increased the membrane headgroup packing of SR phospholipids (Fig. 2g&h), suggesting that PEMT may affect SR-resident ATPases. SERCA is a Ca^{2+} reuptake ion channel that derives its Ca^{2+} pumping energy from ATP hydrolysis. Indeed, SERCA-dependent ATP hydrolysis accounts for the majority of resting metabolic rate in muscle.[20] Previous studies suggest that SR Ca^{2+} uncoupling, like H^+ uncoupling in mitochondria, can increase energy expenditure.[6,21] SERCA transport efficiency (Ca^{2+} uptake/ATP hydrolysis, or Ca^{2+}/P ratio) is affected by the magnitude of Ca^{2+} gradient, SERCA uncoupling peptide sarcolipin (SLN),[6,7,22] as well as membrane phospholipid composition.[8–11] To evaluate whether the elevated mVO_2 in PEMTKO mice is due to SERCA, we indirectly inhibited SERCA by incubating EDL muscles in the presence of Mg^{2+}. Mg^{2+} ions block the ryanodine receptor (RyR) thereby preventing cytosolic Ca^{2+} release, ultimately leaving SERCA with no substrate to transport. Incubation with 10 mM of $MgCl_2$ eliminated the increase in mVO_2 of PEMTKO compared to WT mice, suggesting that the increase in basal mVO_2 is dependent on SR calcium cycling (Fig. 2i).[16] The difference was not explained by changes in protein abundance for RyR, SERCA1, or SERCA2 proteins (Fig. 2j, Supplementary Fig. 2n), protein and/or mRNA levels of known SERCA uncoupling proteins (Fig. 2j, Supplementary Fig. 2o), or mitochondrial calcium handling (Fig. 2k). To more definitively attribute elevated energy expenditure to SERCA, we quantified its transfer efficiency in SR vesicles isolated from skeletal muscle. Across multiple concentrations of free Ca^{2+}, rates for Ca^{2+} uptake and ATP hydrolysis were quantified in the absence and presence of thapsigargin to determine SERCA-dependent and –independent rates (Fig. 2l&m, Supplementary Fig. 3a–l). Ca^{2+}/P

ratio was significantly lower in SR vesicles from PEMTKO compared to WT mice, with greater difference when cytosolic Ca^{2+} was higher (Fig. 2m). Alternatively, RyR channel could leak to induce thermogenesis.[21,23] However, RyR activity was not different between WT and PEMTKO muscles (Fig. 2n), suggesting that this mechanism is unlikely to contribute to elevated basal energy expenditure in PEMTKO muscle. Together, these data implicate SERCA transport inefficiency, and not Ca^{2+}-leak, to be the cellular process contributing toward elevated muscle energy expenditure in PEMTKO mice.

The liver is the predominant systemic source of phospholipids where these molecules are exported to peripheral tissues via VLDL. While PEMT is expressed in multiple tissues, liver contains the highest amount of PEMT among all cell types.[19] Thus, it was unclear whether the muscle phenotype observed in whole-body PEMTKO mice was due to absence of PEMT in liver, or due to intrinsic loss of PEMT in skeletal muscle.[24] First, we assessed PEMT mRNA expression in muscle from lean and obese humans as well as mice fed standard chow and HFD. Strikingly, obesity coincided with elevated PEMT expression in skeletal muscle (Supplementary Fig. 4a&b). These findings are consistent with observations that increased metabolic rate in PEMTKO mice are present only when mice are fed HFD.[13] Next, in order to examine the tissue-specific effect of PEMT deletion, we generated a mouse strain with its *Pemt* gene flanked by *loxP* sites on the exon 3 (PEMTcKO$^{+/+}$ or control mice, Fig. 3a). We then crossed these mice with Alb-Cre mice or tamoxifen-inducible HSA-MerCreMer mice to generate mice with liver-specific (PEMT-LKO) or skeletal muscle-specific (PEMT-MKO) deletion of PEMT (Supplementary Fig. 4c). Both strains were born with normal Mendelian ratio with no apparent defects. Tissue specificity of PEMT deletion was confirmed with quantitative PCR (Fig. 3b, Supplementary Fig. 4d). When challenged with HFD, control and PEMT-LKO mice equally gained lean and fat mass (Fig. 3c, Supplementary Fig. 4e–j). In contrast, skeletal muscle-specific deletion of PEMT protected mice from diet-induced obesity (Fig. 3c, Supplementary Fig. 4e–g,k&l) that was not explained by a difference in food intake (Fig. 3d, Supplementary Fig. 4h). Similar to whole-body PEMTKO mice,[15] PEMT-MKO mice had increased whole-body metabolic rate (Fig 3e&f, Supplementary Fig. 4m), without an increase in physical activity (Fig. 3g). Nevertheless, PEMT-MKO mice were not more cold tolerant compared to controls (Supplementary Fig. 4n). To more definitely exclude liver PEMT in the hypermetabolic phenotype of whole-body PEMTKO mice, we re-expressed PEMT in liver of these mice with AAV8-TBG-PEMT infection. Consistent with findings in PEMT-LKO mice, liver PEMT had no effect on body weight, energy expenditure, activity, or food intake (Supplementary Fig. 4o–r). Together, increased metabolic rate in whole-body PEMTKO mice is not due to the lack of PEMT in liver, but rather due to the loss of PEMT in skeletal muscle. It is noteworthy that unlike PEMTKO[13] or PEMT-LKO mice, PEMT-MKO mice did not develop hepatic steatosis or inflammation (Fig. 3h–j).[13]

We also characterized the consequence of PEMT deletion to skeletal muscle force-generating capacity with a series of *in vivo* and *ex vivo* tests. PEMT-MKO mice did not display deficiencies in their ability to run or grip strength (Fig 3k&l). We also characterized muscle contractile function with electrically-stimulated force production *ex vivo*. There was no difference in twitch force production (Fig. 3m, Supplementary Fig. 5a). Muscles from PEMT-MKO mice exhibited a slight reduction in tetanic force production (Fig. 3n, Supplementary Fig. 5b). Nonetheless, muscles from PEMT-MKO mice did not demonstrate

greater fatigue (Supplementary Fig. 5c), suggesting that reduced force-generating capacity in PEMT-MKO muscles may come from its inability to effectively cycle Ca^{2+} in and out of SR, rather than deficiency in ATP production. There were no differences in the SDH staining, fiber-type, mitochondrial content, or ultra-structure of the mitochondria (Fig. 3o, Supplementary Fig 5d–h). Importantly, in agreement with decreased adiposity, muscles from PEMT-MKO mice were exquisitely insulin-sensitive (Fig. 3p).

To confirm that increased whole-body energy expenditure in PEMT-MKO mice was due to an increase in skeletal muscle metabolic rate, we measured mVO_2 in skeletal muscle from HFD-fed PEMT-MKO and control mice. mVO_2 from PEMT-MKO mice were ~45% greater compared to control mice (Fig. 4a&b). Repeating these experiments in the presence of Mg^{2+} ions abrogated the difference in mVO_2 (Fig. 4b), suggesting that like muscle from PEMTKO mice the energetic demand of SR Ca^{2+}-flux is responsible for increased metabolic rate in skeletal muscle. Consistent with our findings in the whole-body PEMT knockout mice, Ca^{2+}/P ratio was reduced in isolated SR vesicles from PEMT-MKO compared to control mice (Fig. 4c, Supplementary Fig. 6a&b). The phenotype was not explained by different protein or mRNA abundance for RyR, SERCA1 or SERCA2 in skeletal muscle (Fig. 4d, Supplementary Fig. 6c). Meanwhile, in cultured FDB fibers, basal cytosolic calcium concentration was greater in PEMT-MKO mice compared to control (Fig. 4e), likely reflecting SERCA inefficiency. In contrast, there was no difference in 4-CMC-stimulated Ca^{2+} release, suggesting that SR Ca^{2+} reserve is not different between these mice (Fig. 4e). Mass spectrometry analyses revealed differences in SR phospholipid composition between PEMT-MKO and control muscles with a notable decrease in 16:0/22:6-PC (primary product of PEMT[25]) (Fig. 4f&g, Supplementary Fig. 6d&e). Absence of PEMT did not alter UCP1 levels in brown or white adipose tissues (Supplementary Fig. 6f). Together, these data suggest that PE methylation in skeletal muscle modulate SR phospholipid composition, which in turn alters the energetic efficiency of SERCA ion pump.

As obesity coincided with an increase in muscle PEMT expression, we examined the effect of increased muscle PEMT expression on skeletal muscle metabolic rate. For these studies, mice with skeletal muscle-specific overexpression of PEMT were generated. First, we synthesized mice with conditional knock-in of PEMT ($PEMTcKI^{+/+}$), which was accomplished by inserting a *Pemt* cDNA with a preceding stop codon that was flanked with *loxP* sites into a Rosa26 locus (Fig. 4h). These mice were crossed with HSA-$MerCreMer^{+/-}$ mice which produced PEMT-MKI ($PEMTcKI^{+/-}$, HSA-$MerCreMer^{+/-}$) and control ($PEMTcKI^{+/-}$, HSA-$MerCreMer^{-/-}$) mice. Skeletal muscle-specific overexpression of PEMT was confirmed by qPCR (Fig. 4i) which was sufficient to increase SR PC and decrease PE (Fig. 4j&k, Supplementary Fig 7a&b). Consistent with our observation that PEMT deletion increased mVO_2, PEMT overexpression reduced mVO_2 by ~40% (Fig. 4l&m). This occurred in the absence of changes in in SR Ca^{2+} handling proteins (Fig. 4n, Supplementary Fig. 6c). Consistent with data from PEMT deletion, muscles from PEMT-MKI demonstrated increased SERCA transport efficiency (Fig. 4o, Supplementary Fig. 6d&e). Despite exhibiting lower mVO_2 and improved SERCA-transport efficiency, PEMT-MKI and control mice did not differ in whole-body energy expenditure, activity, food intake, or propensity for weight gain on chow or HFD diet (Supplementary Fig. 6f–r). It is unclear why the lower mVO_2 in PEMT-MKI mice was not reflected in lower whole-body VO_2. We

did not detect greater UCP1 proteins in brown and white adipose tissues (Supplementary Fig. 6s). One possibility is that PEMT-MKI mice compensate for reduced resting mVO_2 by increasing muscle shivering or small locomotion not detected by our motion sensor. Nevertheless, these data demonstrate that increased PE methylation is sufficient to decrease skeletal muscle metabolic rate.

Obesity is a major public health problem with at least 2.1 billion overweight people worldwide. Strategies to reduce energy efficiency, especially by means of mitochondrial uncoupling in brown and white adipose tissues,[26] have attracted much attention as mechanisms that increase energy expenditure and decrease propensity for weight gain. While studies on UCP1-dependent thermogenesis in adipose tissues yield a strikingly robust phenotype in mouse models, it is yet unclear how targeting this mechanism would increase energy expenditure in humans. Meanwhile, skeletal muscle represents an organ with substantial contribution for whole-body energy expenditure.[27] Exercise and shivering are two examples in which an increase in skeletal muscle energy expenditure effectively increases whole-body energy expenditure. Skeletal muscle tissues are also anatomically ideally situated for thermogenesis, away from vital organs and well-vascularized to dissipate heat. The current study uncovered a mechanism by which phospholipids alter the energy efficiency of skeletal muscle SERCA to affect propensity for obesity. In humans, skeletal muscle phospholipid metabolism becomes highly affected with obesity or exercise.[28,29] We speculate that these changes may be responsible for alterations in skeletal muscle energy efficiency that are thought to occur with weight fluctuation or exercise training.[30]

Methods

Animal models

C57BL/6J mice (WT) were used as controls for whole-body PEMT knockout mice (PEMTKO).[31] Using a traditional homologous-recombination method, PEMT-conditional knockout (PEMTcKO$^{+/+}$) mice were generated by flanking *Pemt* exon 3 with *loxP* sites. PEMTcKO$^{+/+}$ mice were then crossed with HSA-MerCreMer[32] mice to generate mice with tamoxifen-inducible skeletal muscle-specific knockout of PEMT (PEMT-MKO: PEMTcKO $^{+/+}$, HSA-MerCreMer$^{+/-}$) or with Alb1-Cre[33] mice to generate mice with liver-specific knockout of PEMT (PEMT-LKO: PEMTcKO$^{+/+}$, Alb1-Cre$^{+/-}$), all on a C57BL/6J background. For both PEMT-MKO and PEMT-LKO, PEMTcKO$^{+/+}$, Cre$^{-/-}$ mice were used as littermate controls. PEMT conditional knock-in (PEMTcKI$^{+/+}$) mice were generated by inserting myc-tagged human *Pemt* cDNA with a preceding stop codon that was flanked with *loxP* sites into a Rosa26 locus. PEMTcKI$^{+/+}$ mice were crossed with HSA-MerCreMer mice to generate skeletal muscle specific knock-in of PEMT (PEMT-MKI: PEMTcKI$^{+/+}$, HSA-MerCreMer$^{+/-}$) and littermate controls (PEMTcKI$^{+/+}$, HSA-MerCreMer$^{-/-}$), all on a C57BL/6J background. For some experiments, Cre control mice (PEMTcKO$^{-/-}$ or PEMTcKI$^{-/-}$ with HSA-MerCreMer$^{+/-}$ or Alb1-Cre$^{+/-}$) or tamoxifen-untreated control mice (PEMTcKO$^{+/+}$, HSA-MerCreMer$^{+/-}$ or PEMTcKI$^{+/-}$, HSA-MerCreMer$^{+/-}$ with no tamoxifen), which displayed no difference in phenotype compared to the *control* mice. At 10 weeks of age, PEMT-MKO, PEMT-MKI, and respective controls were injected with tamoxifen 5 consecutive days at a dose of 7.5 μg•g^{-1}. Tamoxifen-treated mice were given a

two-week washout before beginning high fat diet (HFD, 42% fat, Envigo TD.88137) feeding. PEMTKO, PEMT-LKO, and their respective control mice began HFD feeding at 10–12 weeks of age. All mice underwent 8 weeks of HFD feeding and were fasted 4 hours prior to terminal experiments and tissue collection. All mice were born with normal Mendelian ratios. Both male and female mice were studied with no difference in phenotype. All protocols were approved by Institutional Animal Care and Use Committees at East Carolina University and University of Utah.

AAV8 infection

PEMTKO mice were intravenously injected with 4×10^{11} GC of adeno-associated virus 8 (AAV8) expressing either green fluorescent protein (eGFP) or phosphatidylethanolamine methyltransferase (PEMT) regulated by thyroxine-binding globulin (AAV8-TBG-eGFP or AAV8-TBG-PEMT) promoter to drive liver-specific expression of eGFP or PEMT in PEMTKO mice (Vector Biolabs, Malvern, PA, USA). C57BL/6J mice were injected with AAV8-TBG-eGFP. Two weeks after viral injection, mice were fed with HFD for 8 weeks.

Ca^{2+} fluorescence

Flexor digitorum brevis (FDB) muscles were digested in Krebs-Henseleit Buffer (KHB) containing 2 mg/mL collagenase type II (Worthington Biochemical, Lakewood, NJ, USA) for two hours at 37°C. Digested FDB muscles were then transferred to KHB without collagenase or $CaCl_2$ and titrated to separate them into individual muscle fibers. Fibers were plated on laminin coated 96-well plate and allowed to adhere for >30 minutes before experimentation. Fibers were used within 5 hours of dissection. Muscle fibers were loaded with 5 μM Fluo-4-AM (F14201, Invitrogen) and Pluronic F-127 (P3000MP, Invitrogen) in the dark for 30 minutes at room temperature. Fibers were then washed in dye-free solution supplemented with 25 μM N-benzyl-p-toluene sulfonamide (BTS, AAJ64910MA, Fisher Scientific) for 20 minutes to block myosin ATPase. Loaded fibers were imaged using EVOS FL microscope (Life Technologies Corp., Carlsbad, CA, USA). To stimulate Ca^{2+} release from the SR, fibers were injected with 2 mM 4-chloro-m-cresol (4-CMC), a ryanodine receptor agonist. Basal fluorescent measurements occurred in the absence of 4-CMC. Image J was used to trace individual muscle fibers, subtract background, and quantify fluorescence.

Cold tolerance test

Mice received subscapular injection of a wireless temperature transponder (IPTT-300, Bio Medic Data Systems, Seaford, DE, USA). One week following transponder injection, mice were placed in a 4°C room for eight hours with access to food and water. Body temperatures were recorded hourly.

Electron microscopy

Freshly dissected extensor digitorum longus (EDL) was cut into ~2 mm pieces and processed by the Electron Microscopy Core at University of Utah. Muscle pieces were submerged in fixative solution (1% glutaraldehyde, 2.5% paraformaldehyde, 100 mM cacodylate buffer pH 7.4, 6 mM $CaCl_2$, 4.8% sucrose) and stored at 4°C overnight. Samples then underwent 3×10 minute washes in 100 mM cacodylate buffer (pH 7.4) prior to

secondary fixation (2% osmium tetroxide) for 1 hour at room temperature. After secondary fixation, samples were subsequently rinsed for 5 minutes in cacodylate buffer and distilled H_2O, followed by prestaining with saturated uranyl acetate for 1 hour at room temperature. After prestaining, samples were dehydrated with graded ethanol series (2 × 15 minutes each: 30%, 50%, 70%, 95%; then 3 × 20 minutes each: 100%) and acetone (3 × 15 minutes), and were infiltrated with EPON epoxy resin (5 hours 30%, overnight 70%, 3 × 2 hour 40 minute 100%, 100% fresh for embed). Samples were then polymerized for 48 hours at 60°C. Ultracut was performed using Leica UC 6 ultratome with sections at 70 nm thickness and mounted on 200 mesh copper grids. The grids with the sections were stained for 20 minutes with saturated uranyl acetate and 10 minutes with lead citrate. Sections were examined at an accelerating voltage of 120 kV in a JEOL-1400 Plus Transmission Electron Microscope (JEOL, Japan), equipped with CCD Gatan camera.

Histochemistry

Coronal brain sections were taken from WT and PEMTKO mice after a 8-week HFD feeding and immunohistochemistry for POMC (Phoenix Pharmaceuticals, Burlingame, CA, USA) and DAPI (4′,6-diamidino-2-phenylindole, 1 mg ml^{-1}, Sigma Aldrich).[34,35] Liver samples were frozen in Tissue-Tek O.C.T. compound and 10 μm sections were stained with Oil-red O staining or paraffin embedded and 5 μm stained with hematoxylin and eosin (H&E). Samples were imaged on Axio Scan Z.1 (Zeiss). Brown adipose (BAT) and subcutaneous inguinal white adipose tissues (iWAT) were embedded in paraffin and sectioned to 5 μm. Sections were deparaffinized and underwent antigen retrieval prior to overnight incubation with primary antibody for UCP1 (ab23481, Abcam) and subsequent secondary antibody incubation (Alexa Fluor 594, A32740, Invitrogen).

Membrane headgroup packing

Sarcoplasmic reticulum (SR)-enriched fraction was isolated from quadriceps muscle as described below (under *SERCA-dependent Ca^{2+}-uptake and ATPase Activity*).[4] 30 μg of SR protein was added to 900 μL of HBSS (Gibco, 14025076) for a final volume of 1000 μL. In the cuvette, the sample was incubated at 37°C and stirred at 750 RPM. MC540 was added at a final concentration of 200 nM and samples were incubated for 10 minutes prior to excitation at 495 nm and a spectral scan from 550 to 750 nm. Blank measurements were recorded as no sample with MC540 probe at 10 minutes of incubation at 37°C. For peak intensity, the greatest emission value was subtracted from value of blank measurement for respective wavelength.

Metabolic phenotyping

TSE Calorimetry System (Chesterfield, MO) or Columbus Instruments Lab Animal Monitoring System (CLAMS) were used to measure VO_2, RER, food intake, and physical activity. Mice were individually caged and acclimated for over 24 hours in the TSE Calorimetry System prior to collecting data. Body composition was determined using EchoMRI-700 (Echo Medical Systems, Houston, MA, USA) or Bruker Minispec NMR (Bruker, Germany). Metabolic efficiency was calculated by dividing the total energy intake over 8 weeks of HFD feeding energy intake by an increase in body mass or fat mass over the

same period of time. The total energy intake was derived from caloric content of the HFD and the rate of its consumption.

Mitochondrial analysis

Skeletal muscle fiber bundles or mitochondria isolated from hindlimb muscles were analyzed by high-resolution respirometry (Oroboros O2k oxygraphs) and fluorometry (Horiba Fluoromax 3 fluorometers) to quantify ATP production per O_2 reduction (P/O ratio),[36] proton leak,[18] H_2O_2 production,[37] and Ca^{2+} retention.[38] Substrate-dependent oxygen consumption was stimulated by concentrations of: 50 μM palmitoyl-CoA with 5 mM carnitine, 0.5 mM malate, 4 mM ADP, 5 mM pyruvate, 10 mM glutamate, 10 mM succinate, 10 μM cytochrome c, and 0.5 μM FCCP. Reduced glutathione (GSH) and glutathione disulfide (GSSG) were measured using high performance liquid chromatography (HPLC) from gastrocnemius homogenate.[39]

Muscle fiber-typing

Frozen, OCT-embedded hindlimb muscle samples (tibialis anterior, mixed fiber-type) were sectioned at 10 μm using a cryostat (Microtome Plus@). Following 1h blocking with M.O.M mouse IgG blocking (Vector, Cat#MKB-2213), myofiber sections were incubated for 1 h with concentrated BA.D5, SC.71, and BF.F3 (all 1:100; Developmental Studies Hybridoma Bank, University of Iowa) and laminin (1:200; Sigma, Cat#L9393) in 2.5% normal horse serum. To visualize laminin (for fiber border), myosin heavy chain I (MHC I), myosin heavy chain IIa (MHC IIa), and myosin heavy chain IIb (MHC IIb), slides were incubated for 1h with the following secondary antibodies: AMCA (1:250 Vector, Cat#CI-1000), Alexa Fluor 647 (1:250; Invitrogen (Carlsbad, CA), Cat#A21242), Alexa Fluor 488 (1:500; Invitrogen, Cat#A21121) and Alexa Fluor 555 (1:500; Invitrogen, Cat#A21426), respectively. Negative stained fibers were considered myosin heavy chain IIx (MHC IIx). After staining, slides were coverslipped with mounting media (Vector, Cat#H-1000). Stained slides were imaged with a fully automated wide field light microscope (Nikon, Nikon Corp.; Tokyo, Japan) with 10X objective lens. Images were captured using high sensitivity Andor Clara CCD (Belfast, UK).

Muscle force measurements *ex vivo*

Extensor digitorum muscles (EDL) were excised and suspended *ex vivo* in a tissue bath containing KHB + 8 mM glucose at 37°C. EDL were chosen as it can be sutured tendon to tendon and be utilized for highly-reproducible *ex vivo* measurements for force-generating capacity. Muscles were adjusted to optimal resting tension prior to recording twitch, force frequency, or fatigue measurements. Twitch and force frequency measurements were performed[16] and fatigue measurements were assessed by 0.2 ms electrical pulse every 0.5 s for 2 minutes. All measurements were recorded using Aurora Scientific Dynamic Muscle Control software (DMCv5.5) and data were analyzed using Aurora Scientific Muscle Analysis software (DMAv5.3; Aurora Scientific, Aurora, ON, Canada).

Muscle function *in vivo*

High fat diet fed control and PEMT-MKO mice performed a low-intensity treadmill running test[40] and inverted screen test.[41] For treadmill running, fed mice were run for 1 h at 10 m/min, followed by an increase of 2 m/min every 15 min until exhaustion. For the inverted screen test, mice were placed on a screen that was then inverted. Mice were evaluated for their time to hang onto the screen. The test was repeated three times and the mean value for the top two times were reported.

Muscle 2-deoxyglucose uptake

Mice were fasted for four hours before anesthetization and excision of contralateral soleus muscles. Soleus muscles were chosen due to their highly-reproducible *ex vivo* measurements for insulin-stimulated glucose uptake. Muscles were initially incubated in a recovery buffer (KHB with 0.1% BSA, 8 mM glucose, and 2 mM mannitol) at 37 °C for 10 minutes. Following this step muscles were then moved to pre-incubation buffer (KHB with 0.1% BSA, 2 mM sodium pyruvate, and 6 mM mannitol) ± 50 mU/mL insulin for 15 minutes. After pre-incubation muscles were placed in incubation buffer (KHB with 0.1% BSA, 9 mM [^{14}C]mannitol, 1 mM [^{3}H]2-deoxyglucose) ± 50 mU/mL insulin for 15 minutes. Contralateral muscles were used for basal or insulin stimulated measurements. Immediately at the completion of the final 15-minute period, muscles were quickly blotted on ice-cold filter paper, snap-frozen, and stored at −80 °C until analyzed with liquid scintillation counting.[4]

Muscle oxygen consumption

For the measurement of oxygen consumption in isolated whole muscle tissues (mVO_2), EDL muscles were excised and suspended *ex vivo* at a resting tension in a sealed tissue bath (Aurora Scientific, Inc. Model: 801C) containing O_2-saturated KHB (-$CaCl_2$) + 8 mM glucose at 37°C.[16] Change in O_2 saturation was measured with an MI-730 Dip-type O_2 sensor (Microelectrode). mVO_2 was calculated by subtracting the rate of O_2 decline in the absence of muscle (O_2 leak) from the rate of O_2 decline in the presence of muscle. The measurements were taken both under resting and calcium-flux inhibited conditions (+$MgCl_2$ 10 mM). Seahorse platform was used for the measurements of oxygen consumption in isolated muscle fibers (OCR). Flexor digitorum brevis (FDB) muscles were excised and separated into single fibers as described above in *Ca^{2+} fluorescence*. Single fibers were plated onto a coated 24-well Seahorse plate and analyzed utilizing a Mito Stress Test kit (Agilent).[42]

Phospholipidomic analysis

Lipids were isolated using methyl-tert-butyl ether protocol.[43] Lipids were reconstituted in methanol:toluene (9:1). Lipid extracts are separated on an Acquity UPLC CSH C18 1.7 μm 2.1 × 50 mm column maintained at 60 °C connected to an Agilent HiP 1290 Sampler, Agilent 1290 Infinity pump, equipped with an Agilent 1290 Flex Cube and Agilent 6490 triple quadrupole (QqQ) mass spectrometer. Results from LC-MS experiments were collected using Agilent Mass Hunter Workstation and analyzed using the software package Agilent Mass Hunter Quant B.07.00. Lipids are quantitated based on peak area ratios to the

internal standards (330710, Avanti Polar Lipids, Inc.) added to the samples prior to extraction.

SERCA-dependent Ca^{2+}-uptake and ATPase activity

Quadriceps muscle was homogenized [300 mM sucrose, 20 mM HEPES pH 7.4, Halt protease (78430)] and underwent differential centrifugation (10 min @ 1300g, 20 min @ 20000g, 2 hr 15 min @ 180000g)[4] to pellet an SR-enriched fraction, which was resuspended in homogenization buffer. SR-fraction was quantified using BCA protein assay (Pierce, 23225) and 10 μg of SR protein was used in each replicate for SERCA-dependent Ca^{2+}-uptake and ATPase activity assay. SERCA-dependent Ca^{2+} uptake and ATPase activity assays were performed in buffer containing 60 mM HEPES, 200 mM KCl, 15 mM $MgCl_2$, 10 mM NaN_3, 1 mM EGTA, and 0.005% Triton-X with varying concentrations of free calcium and with or without 15 μM thapsigargin. SERCA-dependent measures are calculated by taking the difference of values without thapsigargin to values with thapsigargin [Total (without thapsigargin) – SERCA independent (with thapsigargin) = SERCA-dependent]. Ca^{2+} uptake assay buffer additionally contained 5 mM of $(COOK)_2$. ATPase activity assay buffer additionally contained 10 mM PEP, 1.5 mM NADH, 2.4–4 units of pyruvate kinase/ 3.6–5.6 units lactate dehydrogenases enzymes (Sigma, P0294).

Calcium uptake assay[22] was started by the addition of 4 mM ATP and $^{45}CaCl_2$ (Perkin Elmer, NEZ013001MC) to assay buffer with sample. After incubation for 15 minutes at 37°C with 300 RPM rotation, assay was quenched with the addition of 150 mM KCl and 1 mM $LaCl_3$ and placed on ice. Samples were then filtered on to a 0.22 μm PES membrane filter (Millipore, GPWP02500), rinsed 3 × 5 mL PBS, and processed for scintillation counting. SERCA ATPase activity assay[44] was performed on a 96-well plate reader. The assay was initiated by the addition of 4 mM ATP and the absorbance at 340 nm was recorded every 60 seconds for 30 minutes at 37°C. SERCA transport efficiency was determined by the ratio of SERCA-dependent Ca^{2+} uptake to SERCA-dependent ATPase hydrolysis.

Succinate dehydrogenase (SDH) staining

Muscle sections (see Muscle fiber-typing) were incubated in freshly-made SDH staining solution [0.367 mM nitrotetrazolium blue (N6876, Sigma) and 60 mM succinate acid disodium (224731, Sigma) in 1x PBS pH 7.4 (10010, Gibco)]. Sections were incubated at 37°C for 1 hour. Sections were rinsed in 30%, 60%, and 30% Acetone for 1 minute, followed by a three rinses with distilled H_2O. Sections were then mounted (H-1000, Vector Laboratories) and imaged at 10x using Evos FL light microscope (Life Technologies Corp., CA, USA).

Multiplex analysis

Serum T_3, T_4, and TSH were measured with Milliplex MAP (RTHYMAG-30K, EMD Millipore, Billerica, MA).

Nucleotide analysis

Soleus muscles were freeze-clamped immediately post-dissection. Nucleotides were extracted using perchloric acid and concentrations of ATP, ADP, AMP, and IMP were determined by ultra-performance liquid chromatography.[45]

Quantitative PCR

Total RNA was extracted from tissues using TRIzol (Invitrogen). One μg of RNA was reverse transcribed using iScript cDNA synthesis kit (BioRad). PCR reactions were performed with a Life Technologies QuantStudio 12K Flex instrument using SYBR Green PCR Master Mix. Assays were performed in duplicate and all results were normalized to ribosomal protein L32 mRNA levels, which were unchanged between controls and respective experimental groups. All values were normalized to the mean of the control group. Primers were based on sequences in public databases.

Ryanodine binding assay

The protocol for ryanodine binding was adapted from a previously described method.[46] Quadriceps muscle was homogenized and processed for an SR-enriched fraction (see SERCA-dependent Ca^{2+}-uptake and ATPase Activity). 20 μg of SR-enriched sample was added to ryanodine binding solution with varying calcium concentrations [300 mM NaCl, 50 mM MOPS pH 7.2, 1 mM EDTA, 0.01% BSA, 0.1% CHAPS, 5 nM ^{3}H-Ryanodine (Perkin Elmer, NET950250UC)]. Samples were run with and without 20 μM ryanodine to determine ^{3}H-ryanodine binding. Samples were run in triplicate for 17 hours at 25°C and were rotated at 300 RPM. Samples were then filtered on a 0.22 μm PES membrane filter (Millipore, GPWP02500), washed 3 × 5 mL with PBS, and processed for scintillation counting.

Western blotting

Muscle homogenates were probed for proteins of mitochondrial oxidative phosphorylation (ab110413, Abcam), RyR (sc-13942, Santa Cruz), SERCA1 (ab2819, Abcam), SERCA2 (ab3625, Abcam), SLN (ABT13, Millipore), and GAPDH (2118, Cell Signaling). Brown adipose tissue (BAT), epididymal white adipose (eWAT), or inguinal subcutaneous white adipose tissue (iWAT) were blotted for UCP1 (UCP11-A, Alpha Diagnostic). Additionally, BAT was blotted for COXIV (4844S, Cell Signaling) or Citrate Synthase (ab96600, Abcam).

Statistical analyses

Data are presented as means ± s.e.m. Statistical analyses were performed using GraphPad Prism 7.03 or SigmaPlot 8.0 software. Independent samples t-tests were used to compare two groups. For two-by-two comparisons, two-way ANOVA analyses were performed (main effect of genotype shown with an asterisk over a horizontal line) followed by appropriate post-hoc tests corrected for multiple comparisons. For all tests $P<0.05$ was considered statistically significant.

Reporting Summary

Additional information on experimental design is available in the Nature Research Reporting Summary.

Data Availability

Data that support the findings of this study are available from the corresponding author upon reasonable request.

Supplementary Material

Refer to Web version on PubMed Central for supplementary material.

Acknowledgements

This research is supported by NIH DK107397, DK109888 (to K.F.), DK110656 (to P.D.N.), DK112826, DK108833 (to W.L.H.), DK115824, DK116450 (to S.A.S.), DK103930 (to C.J.V.), AR066660 (to E.E.S.), AR070200 (to J.J.B), HL129362 (to T.E.R.), and DK091317 (to T.S.T.), P&F funding from P30 DK020579 at Washington University in St. Louis (to K.F.), American Heart Association 18PRE33960491 (to A.R.P.V.) and 19PRE34380991 (to J.M.J.), Larry H. & Gail Miller Family Foundation (to P.J.F. and to C.J.V.), and Uehara Memorial Foundation (to H.E.). University of Utah Metabolomics Core Facility is supported by S10 OD016232, S10 OD021505, and U54 DK110858.

References

1. Laganowsky A et al. Membrane proteins bind lipids selectively to modulate their structure and function. Nature 510, 172–175, doi:10.1038/nature13419 (2014). [PubMed: 24899312]
2. Gupta K et al. The role of interfacial lipids in stabilizing membrane protein oligomers. Nature 541, 421–424, doi:10.1038/nature20820 (2017). [PubMed: 28077870]
3. Fu S et al. Aberrant lipid metabolism disrupts calcium homeostasis causing liver endoplasmic reticulum stress in obesity. Nature 473, 528–531, doi:10.1038/nature09968 (2011). [PubMed: 21532591]
4. Funai K et al. Muscle lipogenesis balances insulin sensitivity and strength through calcium signaling. Journal of Clinical Investigation 123, 1229–1240, doi:10.1172/JCI65726 (2013). [PubMed: 23376793]
5. Funai K et al. Skeletal Muscle Phospholipid Metabolism Regulates Insulin Sensitivity and Contractile Function. Diabetes 65, 1–37, doi:10.2337/db15-0659 (2016).
6. Bal NC et al. Sarcolipin is a newly identified regulator of muscle-based thermogenesis in mammals. Nature Medicine 18, 1575–1579, doi:10.1038/nm.2897 (2012).
7. Maurya SK et al. Sarcolipin is a key determinant of basal metabolic rate and its overexpression enhances energy expenditure and resistance against diet induced obesity. Journal of Biological Chemistry 290, jbc.M115.636878, doi:10.1074/jbc.M115.636878 (2015).
8. Caffrey M & Feigenson GW Fluorescence quenching in model membranes. 3. Relationship between calcium adenosinetriphosphatase enzyme activity and the affinity of the protein for phosphatidylcholines with different acyl chain characteristics. Biochemistry 20, 1949–1961, doi:10.1021/bi00510a034 (1981). [PubMed: 6452902]
9. Navarro J, Toivio-Kinnucan M & Racker E Effect of lipid composition on the calcium/adenosine 5'-triphosphate coupling ratio of the Ca^{2+}-ATPase of sarcoplasmic reticulum. Biochemistry 23, 130–135 (1984). [PubMed: 6229280]
10. Lervik A, Bresme F, Kjelstrup S & Rubi JM On the thermodynamic efficiency of Ca^{2+}-ATPase molecular machines. Biophysical Journal 103, 1218–1226, doi:10.1016/j.bpj.2012.07.057 (2012). [PubMed: 22995494]
11. Fajardo VA et al. Dietary docosahexaenoic acid supplementation reduces SERCA Ca^{2+} transport efficiency in rat skeletal muscle. Chemistry and Physics of Lipids 187, 56–61, doi:10.1016/j.chemphyslip.2015.03.001 (2015). [PubMed: 25772907]
12. Sharma NK, Langberg KA, Mondal AK & Das SK Phospholipid Biosynthesis Genes and Susceptibility to Obesity: Analysis of Expression and Polymorphisms. PLoS ONE 8, doi:10.1371/journal.pone.0065303 (2013).

13. Jacobs RL et al. Impaired de novo choline synthesis explains why phosphatidylethanolamine N-methyltransferase-deficient mice are protected from diet-induced obesity. Journal of Biological Chemistry 285, 22403–22413, doi:10.1074/jbc.M110.108514 (2010). [PubMed: 20452975]
14. Tasseva G et al. Lack of phosphatidylethanolamine N-methyltransferase in mice does not promote fatty acid oxidation in skeletal muscle. Biochimica et Biophysica Acta (BBA) - Molecular and Cell Biology of Lipids 1861, 119–129, doi:10.1016/j.bbalip.2015.11.008 (2016). [PubMed: 26603903]
15. Gao X et al. Insufficient glucose supply is linked to hypothermia upon cold exposure in mice lacking phosphatidylethanolamine N-methyltransferase. Journal of lipid research 56, 1701–1710, doi:10.1194/jlr.M059287 (2015). [PubMed: 26113536]
16. Ferrara PJ, Verkerke ARP, Brault JJ & Funai K Hypothermia Decreases O2 Cost for Ex Vivo Contraction in Mouse Skeletal Muscle. Med Sci Sports Exerc 50, 2015–2023, doi:10.1249/MSS.0000000000001673 (2018). [PubMed: 29787474]
17. Li B et al. Skeletal muscle respiratory uncoupling prevents diet-induced obesity and insulin resistance in mice. Nat Med 6, 1115–1120, doi:10.1038/80450 (2000). [PubMed: 11017142]
18. Fisher-Wellman, Kelsey H et al. Pyruvate dehydrogenase complex and nicotinamide nucleotide transhydrogenase constitute an energy-consuming redox circuit. Biochemical Journal 467, 271–280, doi:10.1042/BJ20141447 (2015). [PubMed: 25643703]
19. Cui Z, Vance JE, Chen MH, Voelker DR & Vance DE Cloning and expression of a novel phosphatidylethanolamine N-methyltransferase. A specific biochemical and cytological marker for a unique membrane fraction in rat liver. The Journal of biological chemistry 268, 16655–16663 (1993). [PubMed: 8344945]
20. Smith IC, Bombardier E, Vigna C & Tupling a. R. ATP Consumption by Sarcoplasmic Reticulum Ca2+ Pumps Accounts for 40–50% of Resting Metabolic Rate in Mouse Fast and Slow Twitch Skeletal Muscle. PLoS ONE 8, 1–11, doi:10.1371/journal.pone.0068924 (2013).
21. Ikeda K et al. UCP1-independent signaling involving SERCA2b-mediated calcium cycling regulates beige fat thermogenesis and systemic glucose homeostasis. Nature medicine 23, 1454–1465, doi:10.1038/nm.4429 (2017).
22. Paran CW et al. Reduced efficiency of sarcolipin-dependent respiration in myocytes from humans with severe obesity. Obesity (Silver Spring) 23, 1440–1449, doi:10.1002/oby.21123 (2015). [PubMed: 25970801]
23. Durham WJ et al. RyR1 S-Nitrosylation Underlies Environmental Heat Stroke and Sudden Death in Y522S RyR1 Knockin Mice. Cell 133, 53–65, doi:10.1016/j.cell.2008.02.042 (2008). [PubMed: 18394989]
24. Shields DJ, Agellon LB & Vance DE Structure, expression profile and alternative processing of the human phosphatidylethanolamine N-methyltransferase (PEMT) gene1. Biochimica et Biophysica Acta - Molecular and Cell Biology of Lipids 1532, 105–114, doi:10.1016/S1388-1981(01)00122-6 (2001).
25. Samborski RW, Ridgway ND & Vance DE Metabolism of molecular species of phosphatidylethanolamine and phosphatidylcholine in rat hepatocytes during prolonged inhibition of phosphatidylethanolamine N-methyltransferase. Journal of lipid research 34, 125–137 (1993). [PubMed: 8445336]
26. Kajimura S, Spiegelman BM & Seale P Brown and Beige Fat: Physiological Roles beyond Heat Generation. Cell metabolism 22, 546–559, doi:10.1016/j.cmet.2015.09.007 (2015). [PubMed: 26445512]
27. Zurlo F, Larson K, Bogardus C & Ravussin E Skeletal muscle metabolism is a major determinant of resting energy expenditure. J Clin Invest 86, 1423–1427, doi:10.1172/JCI114857 (1990). [PubMed: 2243122]
28. Lee S et al. Skeletal muscle phosphatidylcholine and phosphatidylethanolamine respond to exercise and influence insulin sensitivity in men. Scientific reports 8, 6531, doi:10.1038/s41598-018-24976-x (2018). [PubMed: 29695812]
29. Newsom SA et al. Skeletal muscle phosphatidylcholine and phosphatidylethanolamine are related to insulin sensitivity and respond to acute exercise in humans. Journal of applied physiology 120, 1355–1363, doi:10.1152/japplphysiol.00664.2015 (2016). [PubMed: 27032901]

30. Ravussin Y, Leibel RL & Ferrante AW Jr. A missing link in body weight homeostasis: the catabolic signal of the overfed state. Cell metabolism 20, 565–572, doi:10.1016/j.cmet.2014.09.002 (2014). [PubMed: 25295786]
31. Walkey CJ, Donohue LR, Bronson R, Agellon LB & Vance DE Disruption of the murine gene encoding phosphatidylethanolamine N-methyltransferase. Proceedings of the National Academy of Sciences of the United States of America 94, 12880–12885, doi:10.1073/pnas.94.24.12880 (1997). [PubMed: 9371769]
32. McCarthy JJ, Srikuea R, Kirby TJ, Peterson C. a. & Esser K a. Inducible Cre transgenic mouse strain for skeletal muscle-specific gene targeting. Skeletal Muscle 2, 8, doi:10.1186/2044-5040-2-8 (2012). [PubMed: 22564549]
33. Yakar S et al. Normal growth and development in the absence of hepatic insulin-like growth factor I. Proceedings of the National Academy of Sciences 96, 7324–7329, doi:10.1073/pnas.96.13.7324 (1999).
34. Huang H et al. Rho-kinase regulates energy balance by targeting hypothalamic leptin receptor signaling. Nature Neuroscience 15, 1391–1398, doi:10.1038/nn.3207 (2012). [PubMed: 22941110]
35. Laing BT, Do K, Matsubara T & Wert DW Voluntary exercise improves hypothalamic and metabolic function in obese mice. doi:10.1530/JOE-15-0510 (2016).
36. Lark DS et al. Direct real-time quantification of mitochondrial oxidative phosphorylation efficiency in permeabilized skeletal muscle myofibers. American Journal of Physiology - Cell Physiology 311, C239–C245, doi:10.1152/ajpcell.00124.2016 (2016). [PubMed: 27335172]
37. Johnson JM et al. Targeted overexpression of catalase to mitochondria does not prevent cardioskeletal myopathy in Barth syndrome. Journal of Molecular and Cellular Cardiology 121, 94–102, doi:10.1016/j.yjmcc.2018.07.001 (2018). [PubMed: 30008435]
38. Gilliam LAA et al. Free Radical Biology and Medicine The anticancer agent doxorubicin disrupts mitochondrial energy metabolism and redox balance in skeletal muscle. Free Radical Biology and Medicine 65, 988–996, doi:10.1016/j.freeradbiomed.2013.08.191 (2013). [PubMed: 24017970]
39. Ferdaoussi M et al. Isocitrate-to-SENP1 signaling amplifies insulin secretion and rescues dysfunctional b cells Find the latest version : Isocitrate-to-SENP1 signaling amplifies insulin secretion and rescues dysfunctional β cells. 125, 3847–3860, doi:10.1172/JCI82498.tive (2015).
40. Gan Z et al. The nuclear receptor PPARβ/δ programs muscle glucose metabolism in cooperation with AMPK and MEF2. Cold Spring Harbor Laboratory Press, 2619–2630, doi:10.1101/gad.178434.111.4 (2011).
41. Zechner C et al. Total skeletal muscle PGC-1 deficiency uncouples mitochondrial derangements from fiber type determination and insulin sensitivity. Cell Metabolism 12, 633–642, doi:10.1016/j.cmet.2010.11.008 (2010). [PubMed: 21109195]
42. Schuh RA, Jackson KC, Khairallah RJ, Ward CW & Spangenburg EE Measuring mitochondrial respiration in intact single muscle fibers. American journal of physiology. Regulatory, integrative and comparative physiology 302, R712–719, doi:10.1152/ajpregu.00229.2011 (2012).
43. Matyash V, Liebisch G, Kurzchalia TV, Shevchenko A & Schwudke D methods Lipid extraction by methyl- tert -butyl ether for high-throughput lipidomics. 49, 1137–1146, doi:10.1194/jlr.D700041-JLR200 (2008).
44. Simonides WS & van Hardeveld C An assay for sarcoplasmic reticulum Ca2(+)-ATPase activity in muscle homogenates. Analytical biochemistry 191, 321–331, doi:10.1016/0003-2697(90)90226-Y (1990). [PubMed: 2150742]
45. Brault JJ, Pizzimenti NM, Dentel JN & Wiseman RW Selective inhibition of ATPase activity during contraction alters the activation of p38 MAP kinase isoforms in skeletal muscle. Journal of Cellular Biochemistry 114, 1445–1455, doi:10.1002/jcb.24486 (2013). [PubMed: 23296747]
46. Aracena-Parks P et al. Identification of cysteines involved in S-nitrosylation, S-glutathionylation, and oxidation to disulfides in ryanodine receptor type 1. Journal of Biological Chemistry 281, 40354–40368, doi:10.1074/jbc.M600876200 (2006). [PubMed: 17071618]

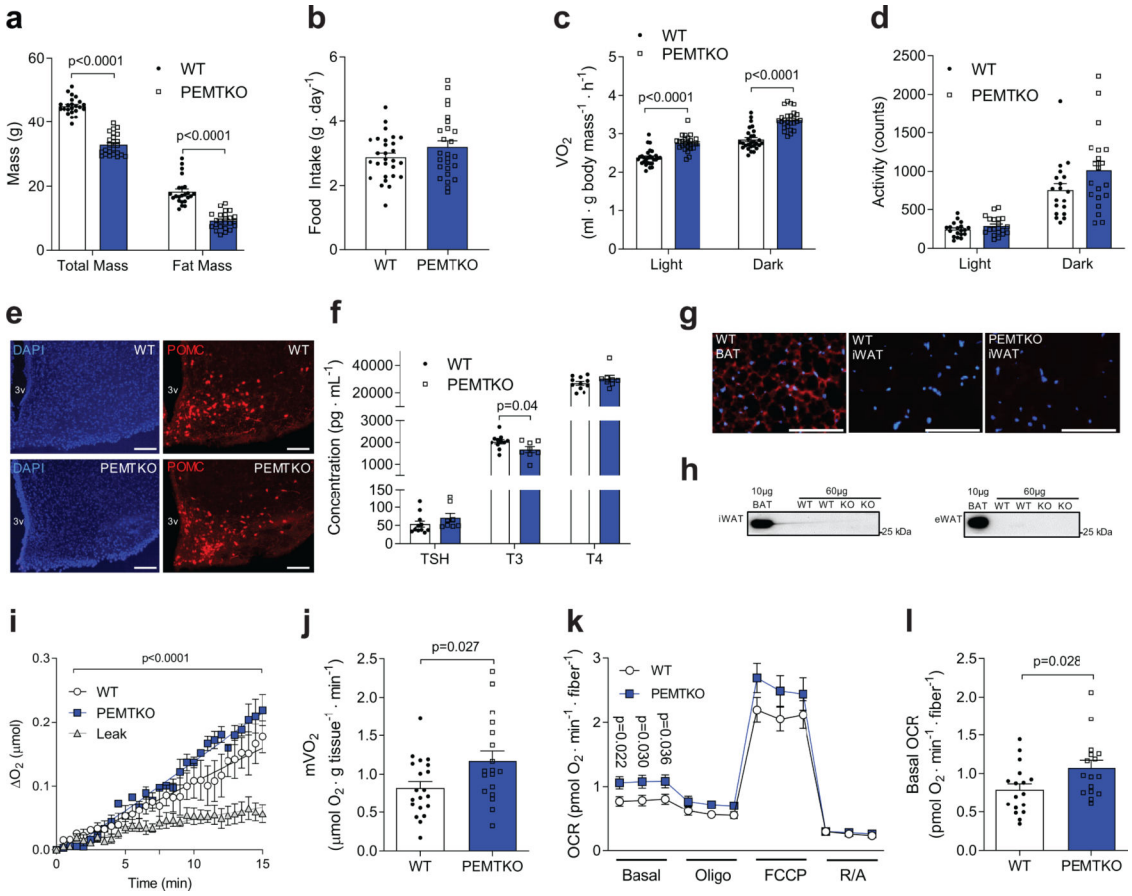

Figure 1.

PEMTKO mice exhibit increased muscle metabolic rate and are protected from diet-induced obesity. (**a**) Body mass and fat mass (n=23 for WT and 24 for PEMTKO), (**b**) food intake (n=28 for WT and 26 for PEMTKO), (**c**) whole-body VO_2 (n=28 for WT and 26 for PEMTKO), and (**d**) activity (n=19 for WT and 20 for PEMTKO) of WT and PEMTKO mice after 8 weeks of HFD feeding. (**e**) Representative images of DAPI and POMC staining in arcuate nucleus of the hypothalamus from 3 mice per genotype, scale bar: 50 µm. (**f**) Thyroid stimulating hormone (TSH), triiodothyronine (T_3), and thyroxine (T_4) serum abundance (n=11 for WT and 8 for PEMTKO). (**g**) Representative immunocytochemical fluorescence images from two independent samples per genotype for DAPI (blue) and UCP1 (red) in WT brown adipose tissue (BAT), WT inguinal subcutaneous adipose tissue (iWAT), and PEMTKO iWAT, scale bar: 100 µm. (**h**) Representative western blots of UCP1 in iWAT and epididymal adipose tissue (eWAT) (n=3 independent samples per genotype). (**i**) Representative O_2 consumption tracing (n=7 for leak, 3 for WT, and 2 for PEMTKO) and (**j**) mean muscle oxygen consumption rate (mVO_2, n=20 for WT and 18 for PEMTKO) in EDL muscles. (**k**, **l**) O_2 consumption in FDB fibers (OCR: oxygen consumption rate, n=17 for WT and 16 for PEMTKO). Data are shown as the mean ± s.e.m. Statistical analyses in **a**,**c**,**f**,**j**,**k**,**l** were performed with an unpaired two-tailed t-test. Statistical analyses in **i** were performed with a two-way ANOVA.

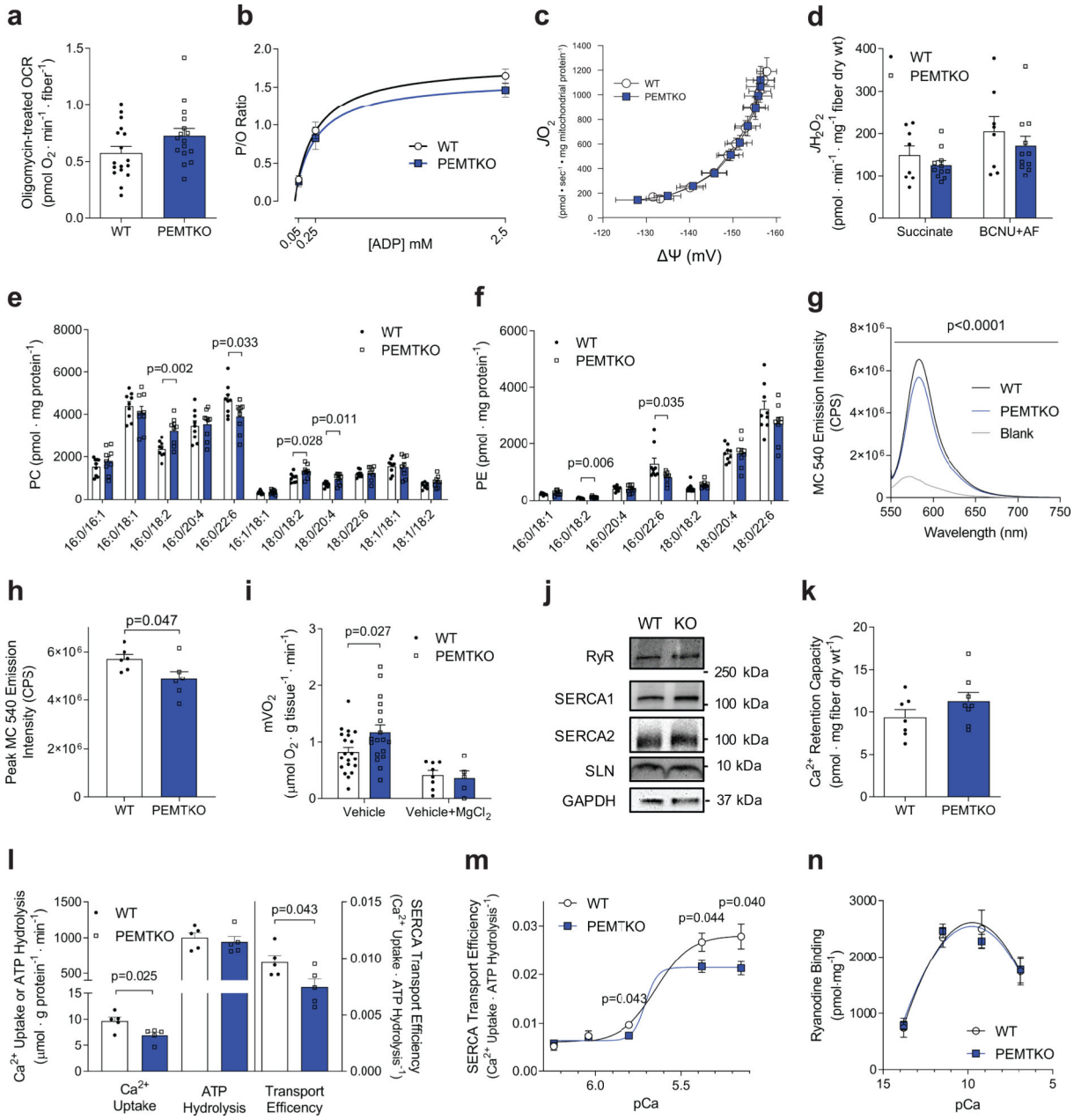

Figure 2.

Ca^{2+} transport inefficiency explains the increased muscle metabolic rate in PEMTKO muscle. (**a**) O_2 consumption of FDB fibers after oligomycin exposure (n=17 for WT and 16 for PEMTKO). (**b**) Mitochondrial ATP production per oxygen reduced (P/O ratio, n=9 for WT and 11 for PEMTKO), (**c**) proton leak (n=9 for WT and 11 for PEMTKO), (**d**) electron leak as estimated by H_2O_2 production in permeabilized gastrocnemius fiber bundles (n=8,11). SR (**e**) phosphatidylcholine (PC) species and (**f**) phosphatidylethanolamine (PE) species (n=9 per genotype). (**g**) SR phospholipid headgroup packing determined by MC540 emission spectrum and (**h**) MC540 peak emission (n=6 per genotype). (**i**) Muscle respiration under resting (vehicle, data from Fig. 1j; n=20 for WT and 18 for PEMTKO) and Mg^{2+}-

stimulated (vehicle+$MgCl_2$, n=8 for WT and 5 for PEMTKO) conditions. (**j**) Protein abundance of RyR (n=8 for WT and 7 for PEMTKO), SERCA1 (n=4 for WT and 4 for KO), SERCA2 (n=8 for WT and 7 for KO), SLN (n=4 for WT and 3 for PEMTKO), and GAPDH. (**k**) Mitochondrial Ca^{2+} retention capacity (n=7 for WT and 8 for PEMTKO). (**l**) SERCA-dependent Ca^{2+} transport, ATP hydrolysis, and transport efficiency (Ca^{2+}/ATP hydrolysis) at pCa 5.8 (n=5 per genotype). (**m**) SERCA-dependent transport efficiency across multiple pCa (n=5 for WT and 6 for PEMTKO at pCa 6.24 and 6.04; n=5 for WT and 5 for KO at pCa 5.8; n=10 for WT and 9 for KO at pCa 5.38; n=12 for WT and 11 for KO at pCa 5.15). (**n**) Ryanodine receptor activity across multiple pCa (n=4 per pCa for each genotype). All results are from 8 week HFD-fed mice. Data are shown as the mean ± s.e.m., with exception of **g** which is shown as mean. Statistical analyses in **e**,**f**,**h**,**i**,**l**,**m** were performed with an unpaired two-tailed t-test. Statistical analyses in **g** were performed with a two-way ANOVA.

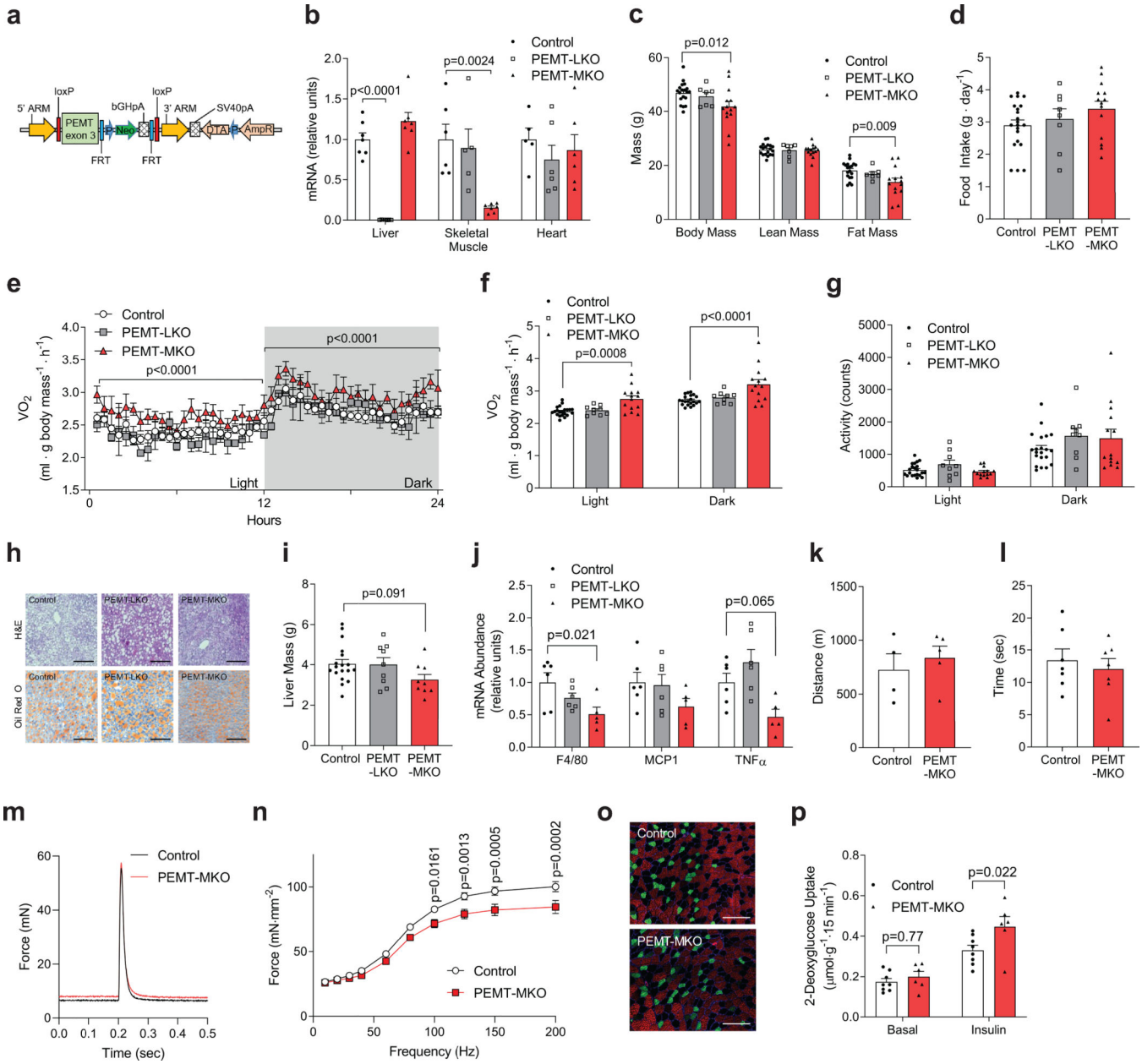

Figure 3.

PEMT-MKO mice are protected from diet-induced obesity. (**a**) A targeting vector used to generate mice with conditional knockout for PEMT. (**b**) mRNA expression of PEMT in liver (n= 7 per genotype), skeletal muscle (tibialis anterior; n=6 for control, 5 for PEMT-LKO, and 7 for PEMT-MKO), and heart (n=5 for control, 6 for PEMT-LKO, and 6 for PEMT-MKO). (**c**) Body mass, lean mass, and fat mass after 8 weeks of HFD feeding (n=19 for control, 7 for PEMT-LKO, and 14 for PEMT-MKO). (**d**) Food intake (n=21 for control, 8 for PEMT-LKO, and 14 for PEMT-MKO), (**e**) representative 24 hour whole-body VO_2 tracing (n= 8 for control, 2 for PEMT-LKO, and 6 for PEMT-MKO), (**f**) mean whole-body VO_2 (n=21 for control, 9 for PEMT-LKO, and 14 for PEMT-MKO), and (**g**) activity (n=21 for control, 9 for PEMT-LKO, and 14 for PEMT-MKO) at 8 weeks of HFD feeding. (**h**)

Representative H&E and Oil Red O staining in liver, scale bar: 200 μm (n=2 independent samples per genotype for H&E and 4 independent samples for Oil Red O). (**i**) Liver mass (n=18 for control, 9 for PEMT-LKO, and 9 for PEMT-MKO) and (**j**) mRNA levels of F4/80, MCP1, and TNFα from HFD fed mice (n=6 for control, 6 for PEMT-LKO, and 5 for PEMT-MKO). (**k**) Treadmill endurance tolerance test (n=4 for control and 5 for PEMT-MKO) and (**l**) inverted screen hang time (n=7 per genotype). (**m**) Representative twitch force tracing (n=10 per genotype) and (**n**) force-frequency curve of tetanic contractions in EDL muscles (n=10 per genotype). (**o**) Representative immunofluorescence images of muscle fiber-type, scale bar: 200 μm (Green: MHC IIa. Red: IIb. No color: IIx. n=5 per genotype). (**p**) 2-deoxyglucose uptake in soleus muscles (n=8 for control and 6 for PEMT-MKO). Data are shown as the mean ± s.e.m., with the exception of **m** which is a representative trace. All results are from 8 week HFD-fed mice. Statistical analyses in **b**,**c**,**i**,**j** were performed with an one-way ANOVA with Dunnett's multiple comparisons test. Statistical analyses in **e**,**f**,**n**,**p** were performed with a two-way ANOVA and multiple comparisons were performed using Tukey's (**f**) or Sidak's (**n**,**p**) multiple comparisons tests.

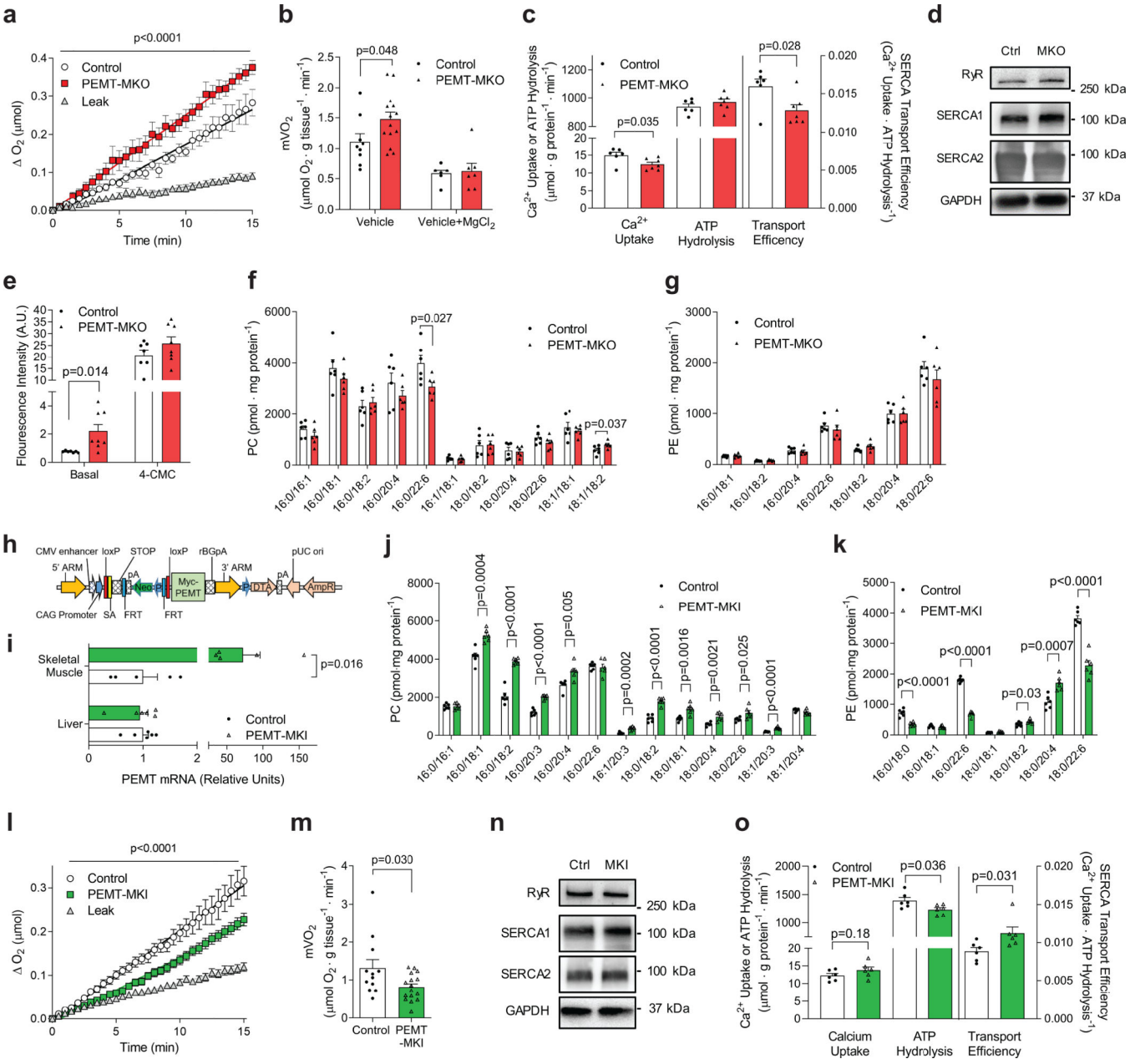

Figure 4.

Skeletal muscle PEMT alters SR phospholipids to regulate muscle oxygen consumption. (**a**) Representative O_2 consumption tracing (n=15 for leak, 7 for control, and 8 for PEMT-MKO) and (**b**) mean mVO_2 under resting (vehicle; n= 9 for control and 14 for PEMT-MKO) or RyR-inhibited (vehicle+$MgCl_2$; n= 6 for control and 7 for PEMT-MKO) conditions in EDL muscles from HFD-fed control and PEMT-MKO mice. (**c**) SERCA-dependent Ca^{2+} transport, ATP hydrolysis, and transport efficiency at pCa 5.8 (n=6 for control and 7 for PEMT-MKO). (**d**) Protein abundance of RyR, SERCA1, SERCA2, and GAPDH in soleus muscles from control and PEMT-MKO mice (n=4 per genotype). (**e**) Fluo-4 fluorescence intensity in basal and 2 mM 4-CMC-stimulated FDB fibers (n=7 for control and 8 for

PEMT-MKO). (**f**, **g**) SR PC and PE in gastrocnemius muscles from control and PEMT-MKO mice (n=6 per genotype). (**h**) A targeting vector used to generate mice with conditional knock-in for PEMT. (**i**) PEMT mRNA levels in liver (n= 6 per genotype) and gastrocnemius muscles (n= 5 per genotype) from control and PEMT-MKI mice. (**j**, **k**) SR PC and PE in gastrocnemius muscles from control and PEMT-MKI mice (n= 6 per genotype). (**l**) Representative O_2 consumption tracings (n=31 for leak, 12 for control, and 16 for PEMT-MKI) and (**m**) mean mVO_2 (n=12 for control and 16 for PEMT-MKI) in EDL muscles from HFD-fed control and PEMT-MKI mice. (**n**) Protein abundance of RyR, SERCA1, SERCA2, and GAPDH (n= 8 per genotype). (**o**) SERCA-dependent Ca^{2+} transport, ATP hydrolysis, and transport efficiency at pCa 5.15 (n=6 per genotype). Data are shown as the mean ± s.e.m. All results are from 8 week HFD-fed mice. Statistical analyses in **b**,**c**,**e**,**f**,**i**,**j**,**k**,**m**,**o** were performed with an unpaired two-tailed t-test. Statistical analyses in **a**,**l** were performed with a two-way ANOVA.